GEODESY AND CARTOGRAPHY
Vol. 70, no. 2, article no. e10, 2021

DOI: https://doi.org/10.24425/gac.2021.136685

Original paper

Part of Topical collection:
"Geodetic techniques in observations of mining deformations and induced seismicity – EPOS-PL"

Assessing the application of GACOS atmospheric correction for DInSAR-based mining deformation monitoring by using Sentinel-1 data in Upper Silesian Coal Basin in Poland

Kamila Pawłuszek-Filipiak*, Natalia Wielgocka, Tymon Lewandowski, Damian Tondaś

Wroclaw University of Environmental and Life Science, Wroclaw, Poland
e-mail: kamila.pawluszek-filipiak@upwr.edu.pl; ORCID: http://orcid.org/0000-0003-2162-371X
e-mail: natalia.wielgocka@upwr.edu.pl; ORCID: http://orcid.org/0000-0002-8420-7046
e-mail: 111809@student.upwr.edu.pl; ORCID: http://orcid.org/0000-0001-5533-4372
e-mail: damian.tondas@upwr.edu.pl; ORCID: http://orcid.org/0000-0001-7922-4469

*Corresponding author: Kamila Pawłuszek-Filipiak, e-mail: kamila.pawluszek-filipiak@upwr.edu.pl

Received: 2021-06-30 / Accepted: 2021-10-13

Abstract: One of the most critical factors which determine the accuracy of deformation maps provided by Differential Synthetic Aperture Radar Interferometry (DInSAR) are atmospheric artefacts. Nowadays, one of the most popular approaches to minimize atmospheric artefacts is Generic Atmospheric Correction Online Service for InSAR (GACOS). Nevertheless, in the literature, the authors reported various effects of GACOS correction on the deformation estimates in different study areas Therefore, this paper aims to assess the effect of GACOS correction on the accuracy of DInSAR-based deformation monitoring in USCB by using Sentinel-1 data. For the accuracy evaluation, eight Global Navigation Satellite Systems (GNSS) permanent stations, as well as five low-cost GNSS receivers were utilized. GACOS-based DInSAR products were evaluated for: (1) single interferograms in different geometries; (2) cumulative deformation maps in various geometries and (3) decomposed results delivered from GACOS-based DInSAR measurements. Generally, based on the achieved results, GACOS correction had a positive effect on the accuracy of the deformation estimates in USCB by using DInSAR approach and Sentinel-1 data in each before mentioned aspect. When considering (1), it was possible to achieve Root Mean Square Error (RMSE) below 1 cm for a single interferogram for only 20% and 26% of the ascending and descending investigated interferograms, respectively when compared with GNSS measurements. The RMSE below 2 cm was achieved by 47% and 66% of the descending and ascending interferograms, respectively.

Keywords: satellite radar interferometry, GACOS correction, deformation maps, mining

1. Introduction

The EPOS project is a Polish realization of the European Plate Observing System (EPOS) initiative, the main goal of which is to integrate existing and newly created research infrastructures to facilitate the use of multidisciplinary data and products in the field of earth sciences in Europe (Mutke et al., 2019). Recent developments in remote sensing technologies open new avenues to study ground surface phenomena. Copernicus programme of European Space Agency (ESA) provides optical and radar remote sensing data to study Earth processes in a completely new way. For the first time, Synthetic Aperture Radar (SAR) images from the Sentinel-1 mission with a remarkable 6 days revisiting time are available for free. Such data allows studying various phenomena such as glaciers, earthquakes, volcanos, landslides, or ground subsidence (Zhou et al., 2009; Przylucka et al., 2015; Winsvold et al., 2018; Ramdani et al., 2019; Razi et al., 2019). Differential SAR Interferometry (DInSAR) by using Sentinel-1 data allows to estimate ground surface deformation with cm-level accuracy with temporal resolution which was not available before. Considering that, one of the main tasks within the EPOS-PL project was to utilize Sentinel-1 data for deformation monitoring over the mining region in Upper Silesian Coal Basin (USCB) in Poland. DInSAR methods are widely used in monitoring mining-induced deformation. More than 20 years ago, the first studies with DInSAR application in USCB in Poland were performed by Perski (1998), which indicated that subsidence in the mining area in USCB can be detected and measured using DInSAR processing. Throughout the years, terrain deformation monitoring in USCB has been studied using different interferometric methods (Graniczny et al., 2014; Przylucka et al., 2015; Pawluszek-Filipiak and Borkowski, 2020) and data from various SAR sensors ranging from the widely used C-band to L- and X-band (Graniczny et al., 2014).

Accuracy of DInSAR-delivered deformation depends on various factors. One of the most critical factors are atmospheric artefacts (Xiao et al., 2021). Atmospheric artefacts are the effect of the propagation delay when microwave signals travel through the two-way pass between the satellite SAR sensor and the Earth's surface (Zebker et al., 1997; Ferretti et al., 2001; Hanssen, 2001). Within atmospheric artefacts, the tropospheric aswell as ionospheric contribution exists. However, the ionospheric artefact has a significant effect in the areas close to the equator (Meyer et al. 2016). Nevertheless, in many cases, the term 'atmospheric effects' is not strictly distinguished from 'tropospheric effects'. Zebker et al. (1997) presented that a 20% change in the relative humidity can cause an error of 10–14 cm. Such an error can lead to misunderstanding of the ground surface processes and strictly depends on the location of the study area, the variability of the atmosphere etc. Although, many scientists attempt to address this problem by providing various atmospheric corrections to DInSAR products.

In the literature, there are different methods to estimate atmospheric disturbances. Among them, mainly three various groups can be distinguished. The first group utilized the relationship between elevation and atmosphere. This method is simple and direct, but the accuracy of this correction is very low (Liu et al., 2020). The second group is based on the statistical analysis (Xiao et al., 2021). Statistical methods utilized statistical

properties of the atmospheric signal, namely, high temporal variability (low temporal correlation) and low spatial variability (high spatial correlation). This assumption is usually applied for multitemporal interferograms in methods such as Small BAseline Subset (SBAS, Berardino et al., 2002) or Persistent Scatterers (PSInSAR, Ferretti et al., 2001). Atmospheric variations are very complex, therefore the assumptions adopted in statistical methods do not often adequately describe InSAR atmospheric artefacts (Xiao et al., 2021). The third group is based on external data, which mainly incorporate ground measurements, satellite-based spectrometer measurement, and numerical weather models. These can provide a relatively independent description of the atmospheric delay field (Xiao et al., 2021). Nonetheless, the availability of auxiliary data, such as Global Navigation Satellite Systems (GNSS) observations and global meteorological model products, facilitates the understanding of the complexity of the InSAR data processing procedure.

Another important aspect, which the scientific community is facing at this moment is the evaluation of these atmospheric corrections, which is made on case-by-case basis (Xiao et al., 2021). Such validation methods can be also be divided into statistical- and ground-truth-based. Statistical evaluation methods are based on several metrics such as the root-mean-square error (RMSE) or standard deviation (StdDev) of the interferometric phase (Murray et al., 2019; Xiao et al., 2021) to assess the performance of the atmospheric correction, with limited attention paid to their applicability and limitations. According to Xiao et al. (2021), certain atmospheric effects, such as distance dependency and elevation dependency, may not be reflected by statistical metrics such as RMSE/StdDev. Murray et al. (2019) present a review of several statistical performance metrics. In contrary, ground-truth evaluation has its limitations connected with the lack of GPS/GNSS stations. Nevertheless, few studies tried to assess the accuracy and performance of atmospheric corrections by 'ground truth', such as the Global Positioning System (GPS) (e.g. Li et al., 2009).

One of the widely used methods based on auxiliary data for atmospheric correction is Generic Atmospheric Correction Online Service for InSAR (GACOS). GACOS was proposed by Chen Yu and colleagues from Newcastle University, United Kingdom, and incorporates GPS observations and weather models (Yu et al., 2017, 2018b, c, 2020). Wide spatial coverage and high temporal and spatial resolution of GACOS products open a new path for increasing the accuracy of DInSAR- delivered deformation maps. Yu et al. (2020) noticed the beneficial effect of GACOS correction in time series analyses, where for 13 months of Sentinel-1 data and GPS station displacements, the RMSE between the observed and modeled surface displacement improved from 2.8 cm with no GACOS correction applied to 0.7 cm with the method using the combination of GACOS corrections and an Atmospheric Phase Screen (APS) filter (Yu et al., 2020). In contrary, Wang et al. (2019) showed that the accuracy of deformation monitoring was improved in the whole investigated study area after GACOS correction, and the mean square error decreased from 0.34 cm/yr to 0.31 cm/yr. However, they realized that even the improvement of the mid-altitude (15–140 m) GNSS measurement station was the most obvious after GACOS correction, the accuracy for low- and high-altitude areas was roughly equal and there was no significant improvement. It shows that the accuracy of GACOS correction in various study areas and settings needs to be further evaluated.

Therefore, considering the area of USCB with its flat surface characteristics, this study aims to evaluate the improvement in accuracy of GACOS-based DInSAR deformation maps in comparison to noncorrected DInSAR-delivered deformation maps based on Sentinel-1 data. For the accuracy evaluation, we utilized the available eight GNSS permanent stations as well as five low-cost GNSS receivers purchased within the EPOS-PL project.

2. Study area

The study area is located in the southern part of Poland (Fig. 1a) and covers about 2690 km^2. It is an area characterized by low ground differences. The maximum altitude difference is about 200 m. The major part is lowland, flat terrain. Higher elevations occur in the north-eastern part of the study area. The area of the study covers the Upper Silesia Coal Basin (USCB). It is one of the largest mining regions in Europe. As a consequence of underground coal mining, the region is characterized by significant ground deformation in the areas of active mining. For this reason, numerous studies are being carried out

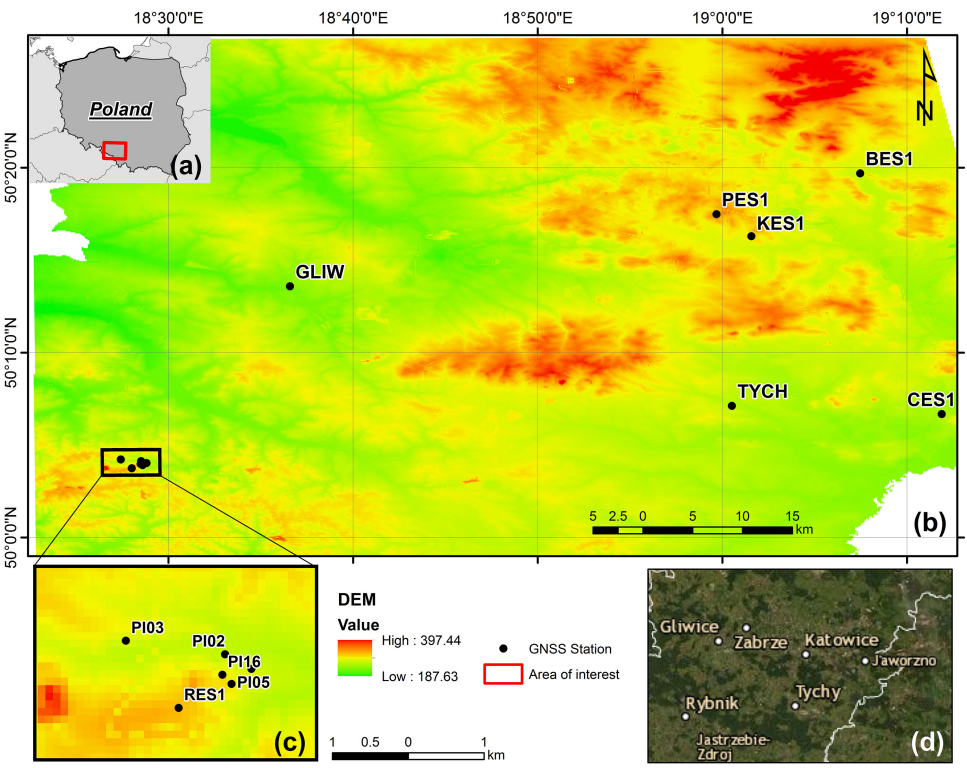

Fig. 1. Location of the study area together with GNSS receivers and Digital Elevation Model (DEM) delivered from Airborne Laser Scanning carried out within the ISOK project in ENRF-2007-NH system: http://www.gugik.gov.pl/

in this area to monitor the magnitude and velocity of these changes (Pawluszek-Filipiak and Borkowski, 2021, 2021). As part of the EPOS-PL project, 13 high-frequency GNSS receivers were placed in the investigated area (Fig. 1b). The highest density of GNSS stations is visible in the south-eastern part of the study area near Rydułtowy Mine (Fig. 1c) where 5 low-cost receivers were placed directly in the area of active mining.

3. Data used

In this study, we used Sentinel-1A/B TOPSAR images acquired between 14th July 2019 and 17th July 2020 in the interferometric wide swath mode (IW). Radar images are in ascending and descending geometry and cover the study area usually with a six-day revisiting period. Moreover, data from the Generic Atmospheric Correction Online Service (GACOS) were used to mitigate atmospheric artefacts. GACOS products contain atmospheric information estimated for the specific day and time. Thus, for each SAR acquisition, GACOS products were acquired. Additionally, the measurements from the Global Navigation Satellite System (GNSS) were used to validate the InSAR results. GNSS measurements as well as SAR data cover the same time period. GNSS deformations were estimated from daily solutions estimated at the post-processing stage. Basic informations about the data used in this study are presented in Table 1.

Table 1. Specification of the data used in this study

Dataset	Parameters	Data specification
Sentinel-1A/B data	Product type	Sentinel-1 SLC IW
	Track number	124
	Orbit mode	descending
	Mean Incidence angle	38.35°
	Azimuth angle	–74.87°
	Number of images	59
	Time span	14th July 2019 to 14th July 2020
	Product type	Sentinel-1 SLC IW
	Track number	175
	Orbit mode	ascending
	Mean incidence angle	40.66°
	Azimuth angle	75.18°
	Number of images	61
	Time span	17th July 2019 to 17th July 2020
GACOS corrections	Time span	14th July 2019 to 17th July 2020
	Number of GACOS images	120
	Source	http://ceg-research.ncl.ac.uk/v2/gacos/
GNSS observation	Number of stations	13
	Time span	14th July 2019 to 17th July 2020

4. Methodology

We estimated the terrain deformation for both geometries using the classical multitemporal consecutive DInSAR method. In the next step, GACOS corrections for the interferogram in ascending and descending geometry have been applied. Afterwards, the accuracy before and after GACOS correction for each interferogram has been compared with the results obtained for 13 GNSS measurements. This evaluation was carried out in the Line of Sight (LOS) direction, therefore the deformations of GNSS stations were reprojected into the LOS ascending and descending geometries, respectively. Secondly, the accuracy of the estimated deformation was evaluated in time by visual inspection of time series charts as well as RMSEs. Finally, the effect of the GACOS correction on the deformation estimates after LOS decomposition in the easting and vertical deformation components was evaluated. These various evaluations will give an entire overview of the GACOS effect on Sentinel-1 based deformation map estimated in USCB. SAR processing was carried out with SNAP software, GACOS corrections were applied using Matlab, and analysis and visualization were carried out in Matlab and ArcGIS. An overview of the full methodology applied in this study is presented in Figure 2 and more detailed descriptions of each step are provided in the following subsections.

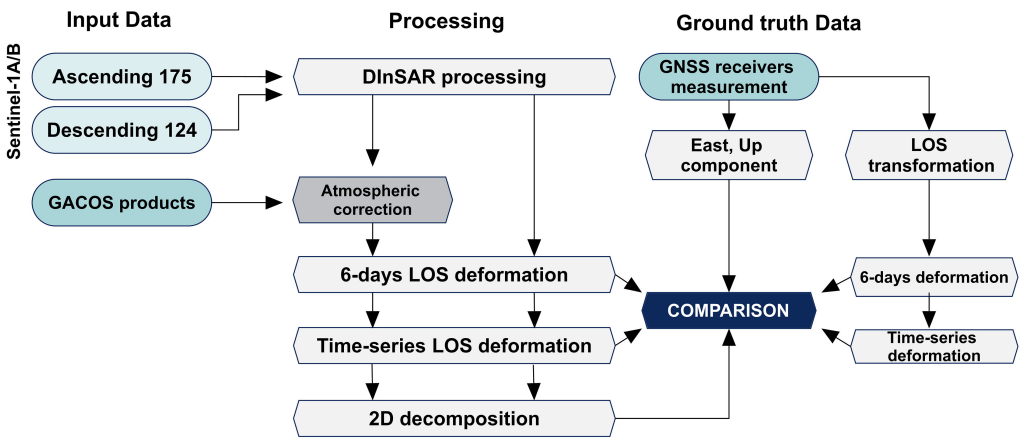

Fig. 2. Methodology flowchart utilized in the presented study

4.1. GNSS processing

The GNSS monitoring of ground surface displacements has been performed based on observations obtained from the ground network of permanent stations. Using over a one-year investigation time span (from July 2019 to July 2020), a daily calculation scheme was established. The estimation process of the GNSS observations was performed in a post-processing service developed within the EPOS-PL project. The post-processing service was based on Bernese GNSS Software v.5.2 (Dach et al., 2015), using observations from multi-GNSS satellite systems: GPS, GLONASS and Galileo. To ensure the high-

est quality of the solution, the final products (orbits, satellite clocks, and Earth rotation parameters) were obtained from the CODE (Center for Orbit Determination in Europe, Bern, Switzerland) (Dach et al., 2018).

The troposphere processing setups were based on a minimum constrained solution with no relative constraining on troposphere parameter estimates. The service used the a priori Zenith Total Delay (ZTD) from The Vienna Mapping Function 1 (VMF1) model for the estimation of site-specific troposphere parameters with VMF1 mapping coefficients (Boehm et al., 2006). For the estimation of ZTD horizontal gradients, Chen and Herring (1997) mapping function was applied.

In the post-processing service double-difference (DD) method was used to calculate observations from 38 stations located in Poland and neighboring countries. From the total number of stations, 25 sites belonged to the global IGS (International GNSS Service) or European EPN (EUREF Permanent GNSS Network) networks and were used as the reference data sources. The remaining 13 stations were located in the area of USCB and were the basic source to evaluate SAR-based deformations (Table 2). In some investigated periods, the low-cost GNSS receivers have not recorded GNSS observations, therefore sometimes there are some breaks within the time series.

Table 2. Specification of the data used in this study

grade	Station ID	Latitude	Longitude	Height [m]
Geodetic	BEDZ	50° 20′ 40.33″	19° 09′ 33.72″	315.202
	BES1	50° 19′ 41.91″	19° 07′ 27.69″	310.612
	CES1	50° 06′ 40.56″	19° 11′ 52.69″	297.907
	GLIW	50° 13′ 35.22″	18° 36′ 34.99″	284.029
	KES1	50° 16′ 17.73″	19° 01′ 34.12″	339.912
	PES1	50° 17′ 29.41″	18° 59′ 40.76″	362.296
	RES1	50° 03′ 44.81″	18° 28′ 00.74″	350.471
	TYCH	50° 07′ 07.48″	19° 00′ 30.92″	306.668
Low-cost	PI02	50° 04′ 07.82″	18° 28′ 31.33″	303.008
	PI03	50° 04′ 13.31″	18° 27′ 25.33″	308.338
	PI04	50° 04′ 01.68″	18° 28′ 48.84″	309.099
	PI05	50° 03′ 55.17″	18° 28′ 35.75″	320.994
	PI16	50° 03′ 59.06″	18° 28′ 29.64″	330.509

The low-cost GNSS stations are permanent stations that use cheaper receivers and antennas instead of geodetic-grade equipment. Similarly to other GNSS stations (8 stations) created within EPOS-PL project, observations from these stations are used only to evaluate DInSAR results and they do not participate in GACOS corrections calculation. In the literature, the accuracy of low-cost stations, using the DD method was established at the 1–2 cm level (Biagi et al., 2016; Notti et al., 2020; Wielgocka et al., 2021).

However, in the performed post-processing calculations, for the analyzed low-cost stations, no significantly larger errors of coordinate determination were found in com-

parison to geodetic-grade GNSS equipment. In general, the mean error of deformation determination was established as 2–4 mm for the horizontal components and 4–7 mm for the vertical component.

4.2. DInSAR processing

In Classical DInSAR methods is based on calculation the phase difference $\delta\phi_j$ between two SAR images ($\phi(t_B)$, $\phi(t_A)$) acquired at two different times, which is represented by the following expression (Hanssen, 2001):

$$\delta\phi_j = \phi(t_B) - \phi(t_A) \approx \frac{4\pi}{\lambda}\left[d(t_B) - d(t_A)\right] + \frac{4\pi}{\lambda}\frac{B_\perp \Delta z}{R\sin\theta} + \left[\phi_{\text{atm}}d(t_B) - \phi_{\text{atm}}d(t_A)\right] + \Delta_{n_j}, \quad \forall j = 1,\ldots,M, \tag{1}$$

where λ is a sensor wavelength, $\phi(t_B,x,r)$ and $\phi(t_A,x,r)$ are the phases that correspond to times t_A and t_B, $d(t_B,x,r)$ and $d(t_A,x,r)$ are the radar LOS projection of cumulative deformation, Δz corresponds to topographic error, $\phi_{\text{atm}}d(t_B,x,r) - \phi_{\text{atm}}d(t_A,x,r)$ reference as atmospheric phase component between two images (A, B), $B_\perp$ is a perpendicular baseline between two acquisitions, R is range distance, θ is incidence angle, and Δ_{n_j} is noise and decorrelation effect.

For the DInSAR, the Sentinel-1 data were processed using a conventional consecutive approach using the smallest temporal six-day temporal baseline (e.g. φ_{1-2}, φ_{2-3}, φ_{3-4}, …, $\varphi_{n-1,n}$). Differential interferograms of the subsequent SAR acquisitions were calculated and accumulated to provide complete time-series interferometric results. The smallest temporal baselines allow to minimize temporal decorrelation and therefore provide better spatial coverage of the DInSAR results. Interferograms have been calculated using SNAP software by using SRTM 1 sec Digital Elevation Model. Due to the lack of two SAR images from the descending orbit for 27th February 2020 and 10th March 2020, two interferograms were calculated with 12-day interval while the others were calculated with 6-day revisiting intervals. Interferograms have been filtered with Goldstein spatial filtering with 3 pixel window size and 64 fast Fourier transform window size. Phase unwrapping has been carried out with Minimum Cost Flow function in snaphu.

4.3. GACOS atmospheric corrections

As shown in Eq. (1), the differential interferometric phase contains some components that are not strictly related to the deformation and influence the accuracy of DInSAR results. Therefore, atmospheric component $\phi_{\text{atm}}d(t_B) - \phi_{\text{atm}}d(t_A)$ in Eq. (1) has been estimated using Generic Atmospheric Correction Online Service for InSAR (GACOS). GACOS was created by Yu et al. (2017, 2018a, b) and is essentially based on numerical weather models and GPS observations. The service is becoming increasingly popular among researchers and since its launch more than 61 000 tasks have been provided

worldwide (Xiao et al., 2021). This was mainly because the tests carried out by the service's developers showed that it was possible to achieve an accuracy of 1 cm compared to ground-truth data (Yu et al., 2018c).

The GACOS products are based on the implementation of an iterative tropospheric decomposition model (ITD) where the stratified and turbulent components are separated by tropospheric delays. As a consequence, high spatial resolution zenith total delay (ZTD) maps are generated in near real-time and for free. The ITD model is described as follows (Yu et al., 2017):

$$\mathrm{ZTD}_k = T\left(x_k\right) + L_0 e^{-\beta \underline{h}_k} + \varepsilon_k\,, \tag{2}$$

where T is the turbulence signal interpolated using the inverse distance weighting method, xk represents the station coordinate vector in the local geocentric coordinate system, L_0 is the stratified component delay at sea level for the selected region and the exponential function with coefficient β represents the stratified component. $\underline{h}_k$ means scaled height defined as $\underline{h}_k = (h_k - h_{\min})/(h_{\max} - h_{\min})$. ε_k is the unmodeled residual error which includes stratified and turbulent signals (Wang et al., 2019).

For GACOS products generation, Digital Elevation Model (DEM) from Shuttle Radar Topography Mission (SRTM) covering the area from 60° S latitude to 60° N latitude are used along with the global digital elevation model from Advanced Spaceborne Thermal Emission and Reflection Radiometer (ASTER) which covers the area 60° S to 83° S and 60° N to 83° N. GACOS uses weather model delivered by European Centre for Medium-Range Weather Forecasts (ECMWF) with 0.125° spatial and 6h temporal resolutions (Wang et al., 2019). Due to the fact that GACOS product represents delays in zenith direction and differential interferogram represents the phase difference in LOS direction, the GACOS product must be converted to LOS using formula (Wang et al., 2019):

$$\phi_{\mathrm{GACOS}} = \frac{4\pi}{\lambda} * \mathrm{GACOS}/\cos\theta_{\mathrm{inc}}\,, \tag{3}$$

where λ is radar wavelength, GACOS is delay map for selected area and θ_{inc} represents radar incidence angle. With delay maps in LOS direction, the atmospheric correction of the interferogram can be calculated. Correction at pixel $(x,\ y)$ is defined as (Wang et al., 2019):

$$\delta\phi_{\mathrm{GACOS},a,b}(x,y) = \phi_{\mathrm{GACOS},b}(x,y) - \phi_{\mathrm{GACOS},a}(xy), \tag{4}$$

where a and b represent different times of SAR image acquisition that compose the interferometric pair and $b > a$. Finally, the corrected interferogram is obtained by calculating the difference between the interferogram and the atmospheric correction map. Within the GACOS correction, it is also possible to apply trend removal as an effect of long-term atmospheric influence. However, in the presented study, we utilized only the corrections provided by GACOS service without trend removal.

4.4. LOS measurement decomposition

The resulting displacement estimated with SAR is represented as a 1D deformation along the LOS direction, which is a combination of vertical (d_u) easting (d_e) and northing (d_n) deformation components as shown in Eq. (5) (Hanssen, 2001):

$$d_{\mathrm{LOS}} = d_u \cos(\theta_{\mathrm{inc}}) - \sin(\theta_{\mathrm{inc}}) \left[d_n \cos\left(\alpha_h - \frac{3\pi}{2}\right) + d_e \sin\left(\alpha_h - \frac{3\pi}{2}\right) \right], \quad (5)$$

where d_{LOS} is the deformation along the LOS direction, α_h is the heading (azimuth) angle, and θ_{inc} is the incidence angle. Based on Eq. (5) theoretically, it is possible to calculate d_u, d_e d_n from the LOS deformation in at least three various geometries. However, the sensitivity of SAR sensors in terms of measuring d_u, d_e and d_n can be represented as (Ng et al., 2011):

$$\begin{bmatrix} \cos(\theta_{\mathrm{inc}}) & -\sin(\theta_{\mathrm{inc}})\cos(\alpha_h) & -\sin(\theta_{\mathrm{inc}})\sin(\alpha_h) \end{bmatrix} \begin{bmatrix} d_u \\ d_e \\ d_n \end{bmatrix} = d_{\mathrm{LOS}}\,. \quad (6)$$

Based on Eq. (6), in the case of an ascending geometry with an incidence angle of 40.66° and an azimuth angle of 75.18°, the coefficients are 0.76, 0.63, and 0.18 for the vertical, easting and northing deformations, respectively. This means that it is impossible to fully capture maximal deformation gradient by using this geometrical SAR settings. Additionally, the contribution of the northing displacement to the total LOS displacement is insignificant (0.09), and since there is a lack of variety in the geometric configurations of different SAR missions, it is very difficult to measure the northing deformation accurately (Ng et al., 2011). In view of the low sensitivity of the northing component, only the vertical and east-west deformation components were estimated by assuming northing deformation component as zero. An interpolation of the deformation over time was also needed, since the image acquisition dates were different in each viewing geometry (with offsets of two and three days). When interpolating the deformation over time, we assumed a linear relationship in time between two consecutive acquisitions (e.g. 6 or 12 days).

Additionally, due to the fact that the displacement estimated with SAR is in the LOS direction, combination of vertical (d_u) easting (d_e) and northing (d_n) deformation components from the GNSS solution was also reprojected onto the LOS direction as shown in (Hanssen, 2001):

$$\begin{aligned} d_{\mathrm{LOS\_}RL} = {} & d_u \cos(\theta_{\mathrm{inc}}) \\ & - \sin\sin(\theta_{\mathrm{inc}}) \left[d_n \cos\cos\left(\alpha_h - \frac{3\pi}{2}\right) + d_e \sin\sin\left(\alpha_h - \frac{3\pi}{2}\right) \right] \end{aligned} \quad (7)$$

where $d_{\mathrm{LOS\_}RL}$ is the deformation along the LOS direction, RL is the relative orbit number, θ_{inc} and α_h represent the value of the incidence angle and the azimuth angle of analyzed ascending and descending orbits, respectively. Conversions between 3D measurements of GNSS were necessary to evaluate the accuracy of DInSAR measurements.

4.5. DInSAR product evaluation

Results of GACOS correction are evaluated in three steps. The first was the inspection of the histogram shape and parameters. More specifically, the statistics and distributions of the histograms were compared with histograms of the interferogram before and after GACOS corrections. The second step was the comparison of the estimated deformation from SAR with GNSS measurements in LOS geometry (Section 4.4). Single interferogram as well as time series was analyzed separately for two viewing geometries to assess the level of improvement for every single geometry.

Pixels corresponding to GNSS station location were extracted from the images. The nearest pixel which contains GNSS station coordinates was selected. The accuracy analysis was performed using the RMSE value. For single interferograms, RMSE was calculated based on the difference in displacement value between the GNSS values and the DInSAR values, according to Eq. (8). RMSE was calculated for the original DInSAR results as well as for the GACOS corrected DInSAR results.

$$\mathrm{RMSE1}_{\mathrm{GNSS\text{-}DInSAR}} = \sqrt{\frac{1}{S}\sum_{i=1}^{s}\left(d_{\mathrm{GNSS}} - d_{\mathrm{DInSAR}}\right)^2} \tag{8}$$

where S is number of GNSS stations, d_{GNSS} represents LOS deformation estimated from GNSS solution and d_{DInSAR} means LOS deformation determined from DInSAR (with and without GACOS correction).

The errors corresponding to time series cumulated deformation for particular GNSS stations were also analyzed. The differences between GNSS and DInSAR values (with and without GACOS) were compared for each SAR acquisition. In this case, RMSE was calculated based on the following equation:

$$\mathrm{RMSE2}_{\mathrm{GNSS\text{-}DInSAR}} = \sqrt{\frac{1}{N}\sum_{i=1}^{N}\left(d_{\mathrm{GNSS}} - d_{\mathrm{DInSAR}}\right)^2} \tag{9}$$

where N is the number of SAR scenes.

Afterwards, the additional question arises how GACOS corrected interferograms influence east-west and up deformation components after LOS decomposition. Therefore, based on Eq. (5) presented in Section 4.4, the results from ascending and descending geometry were reprojected into vertical and easting deformation components and compared with GNSS results.

5. Results

5.1. Single deformation map refinement with the GACOS corrections

A series of 61 interferograms for the ascending orbit and 59 for the descending orbit were generated and corrected with GACOS. Examples representing the original interferograms, GACOS correction, and corrected interferograms are presented in Figure 3.

Moreover, to better understand the influence of the GACOS influence, histograms for the interferograms before and after correction are also presented in Figures 3a4–d4.

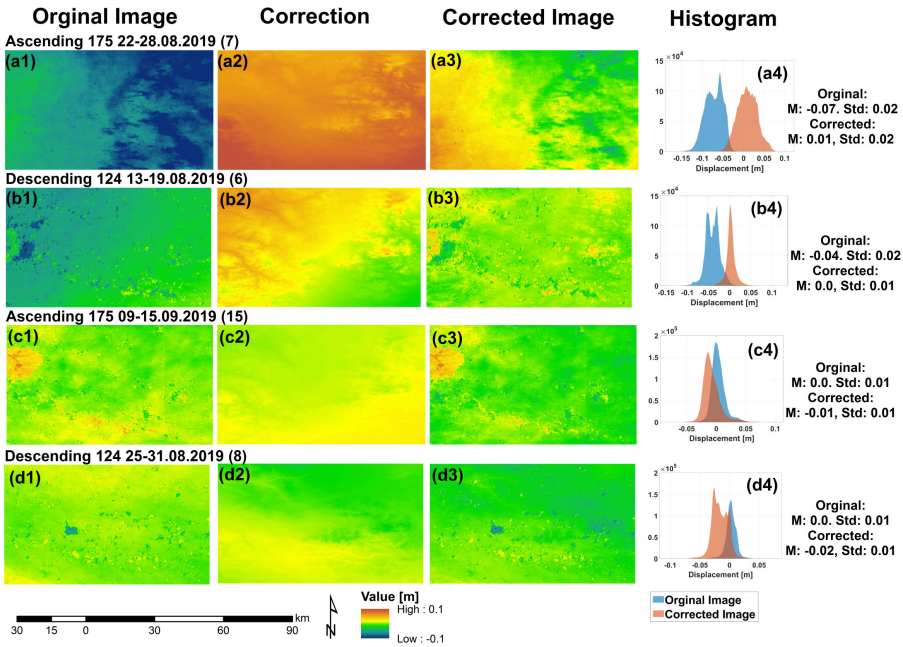

Fig. 3. Examples of original interferograms from DInSAR (a1–d1), the corresponding GACOS correction (a2–d2), and corrected deformation maps masked with the forest areas captured from Corine Land Cover (a3–d3)

These examples were selected to present different scenarios of the GACOS influence on the interferograms. The first example for the ascending orbit (Fig. 3a), shows that GOCOS correction improves the quality of the interferogram. Most of the atmospheric influence over the whole image has been subtracted. The histogram after correction shows values that oscillate within ± 5 cm, while before the correction it was -15 cm to -5 cm. The histogram distribution is close to the normal ones and the mean value of the histogram is zero (Fig. 3a4). The second example (Fig. 3b) is related to the descending orbit. In this case, the influence of the atmosphere is not as much significant as it was observed in the previous example in Fig. 3a. Nevertheless, a global trend which can be observed in Figure 3b2 was removed and the final histogram of the corrected image is close to the normal distribution and the mean value close to 0 (Fig. 3b4). Figure 3c shows an example, where the GACOS correction has even negative effect on the interferograms. A slight shift of the histogram with a mean value of -0.01 can be observed for the corrected image in comparison with the original image (Fig. 3c4). Finally, a clear negative effect of the GACOS correction is shown in Figure 3d. In this case, the GACOS correction introduced some trends in the lower part of the interferogram and the histogram's shape close to the normal distribution has changed to a less regular shape with a mean value of -0.02.

Besides the visual interpretation of the interferograms and histograms, external data from GNSS were used to evaluate the atmospheric correction results. GNSS measurements allowed to evaluate the accuracy of DInSAR-delivered deformation in LOS direction for each single interferogram. This evaluation was carried out separately for GNSS stations with geodetic grade and for low-cost receivers since these two types of stations are characterized by slightly different system specifications and therefore can have diverse accuracy. The obtained RMSE values are presented in Figure 4. Additionally, a green dotted line indicates the value of 1 cm, which represents the error declared by the GACOS developers (Yu et al., 2018a).

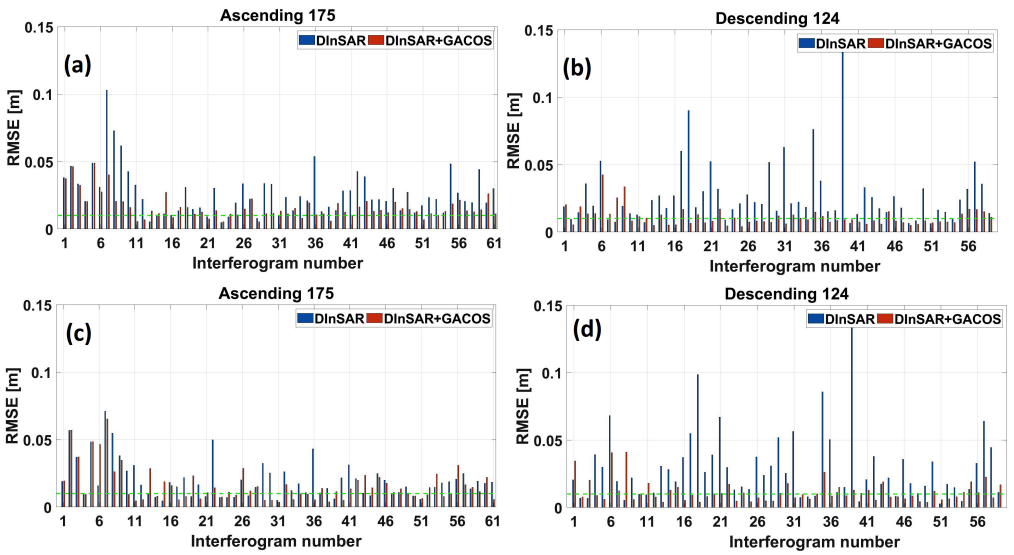

Fig. 4. RMSE for single interferograms at GNSS stations with geodetic-grade (a, b) and low-cost (c, d) receivers

As clearly presented, RMSE calculated for each interferogram for the geodetic grade GNSS station and low cost corresponds to each other quite fairly (Fig. 4). Generally, when observing Figure 4, in most of the interferograms, the correction allowed to reduce the value of the RMSE. For the ascending orbit, the RMSE values oscillate around the declared value of 1 cm. The maximum RMSE after correction is about 4 cm. By applying the GACOS correction, it was possible to reduce destructive atmospheric effects. In extreme cases such as interferogram no. 39 (in descending geometry), RMSE has decreased from 14 cm for the original data to about 1 cm. For the interferograms in the ascending geometry, the atmospheric influences were considerably lower. In this case, the correction also reduced RMSE to a value of about 1–2 cm. Nevertheless, it is worth noting that in some cases the atmospheric corrections introduce additional errors, resulting in an increase of RMSE value. An example is the interferogram no. 15 from the ascending orbit and no. 8 from the descending orbit, whose histogram and correction values are illustrated in Figure 4c and Figure 4d. In summary, based on the investigated

GNSS measurements, it was possible to achieve RMSE below 1 cm for only 20% and 26% of the ascending and descending investigated interferograms, respectively. When considering the RMSE below 2 cm, these values increase to 47% and 66% for the descending and ascending interferograms, respectively.

5.2. Evaluation of the GACOS influence on deformation time series

For the time series of Sentinel-1 acquisitions, GNSS measurements were extracted and reprojected into the LOS direction of each Sentinel-1 geometry (Fig. 5, Fig. 6). It can be

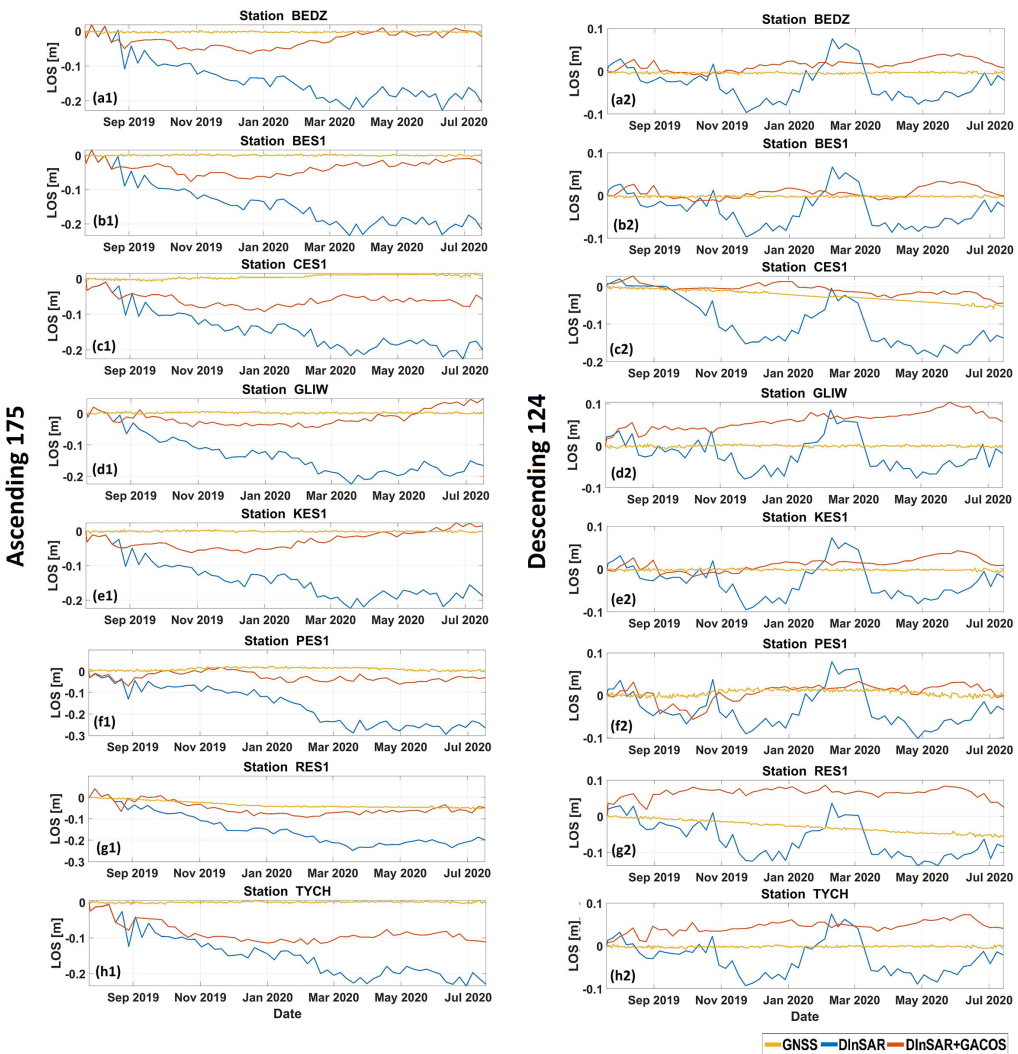

Fig. 5. Time-series in LOS direction from GNSS (yellow line), original DInSAR results (blue), and corrected DInSAR (red) deformation on GNSS station with geodetic grade receivers

seen that GNSS stations with geodetic grade, except for station RES1, are stable. Station RES1 showed small displacements at the level of 3–4 cm/yr. All low-cost GNSS receivers are located in the surroundings of RES1 (Fig. 1c). They also tend to show deformations related to underground mining activities in the area. The rate of these changes is larger than for the RES1 station and for the PI03 station it achieves an even the value of 40 cm/yr in the LOS direction.

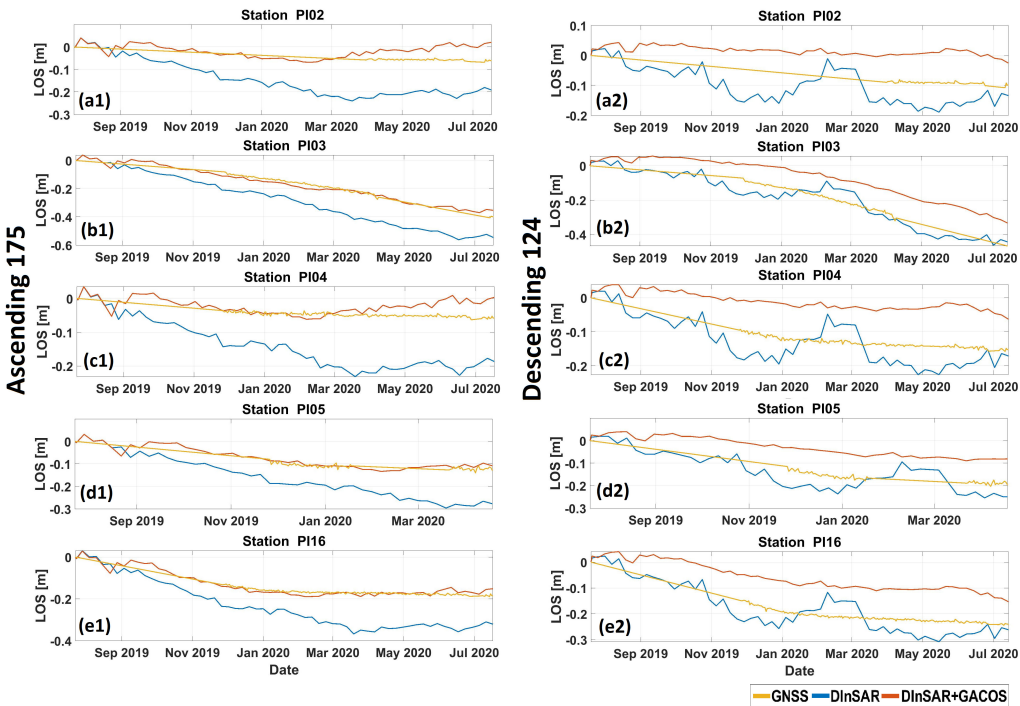

Fig. 6. Time-series in LOS direction from GNSS (yellow line), original DInSAR results (blue) and corrected DInSAR (red) deformation on GNSS station using low-cost receivers. In some cases straight line can be notice in the time series for low-cost which corresponds to breaks in the GNSS measurements which were interpolated using linear model

Due to the different timing of the SAR acquisitions at each orbit (difference is 3 days), the atmosphere has a various impact on these two geometries. For the ascending orbit, an increasing deviation of the original DInSAR solution from the GNSS results can be observed in each time series (Fig. 5a1–h1 and Fig. 6a1–e1), however, this deviation is systematic. Atmospheric errors are accumulated in time and overestimation of the deformation can be observed (Fig. 6a1–e1). After the application of GACOS corrections, the time series are smoothed out and close to the GNSS time series (red line). For a descending orbit, the atmospheric effects have a different character. Accumulated atmospheric errors are not systematic and has some pits and hills mostly around January and March. For all stations, an increased atmospheric impact is seen in the period between

October 2019 and April 2020. The GACOS correction has eliminated these influences and made the time series smoother than before.

Besides the time series, the variation between DInSAR and GNSS measurements were compared in time by calculating RMSE for each station in time (Eq. (9)). This means RMSEs were calculated between GNSS-DInSAR differences for each time, when SAR data have been captured (Fig. 7).

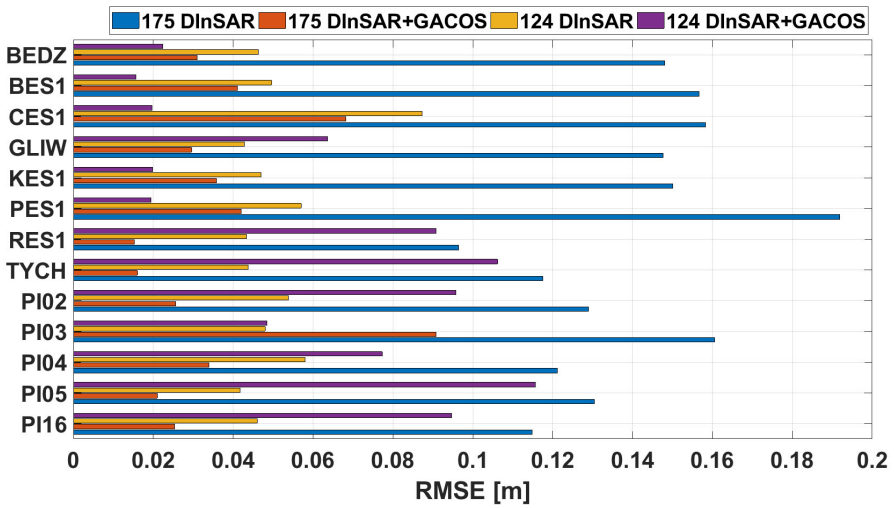

Fig. 7. RMSE for time-series results in ascending 175 and descending 124 geometries for each GNSS measurement

Figure 7 with the RMSE calculated in time, shows that the GACOS correction had a beneficial effect on the accuracy for all stations investigated for the ascending geometry with relative orbit 175. For the interferograms in this geometry, the atmospheric effect had a more destructive impact on the accuracy in time series than on results in descending geometry. The RMSE of the estimated deformation for the DInSAR results without GACOS correction exceeded 9 cm for each GNSS station. After GOCOS correction, the error significantly decreased for each station. For a descending geometry with relative number of 124, RMSEs oscillate between 2 and 9 cm. For the descending geometry, GACOS correction allowed to decrease the RMSE value in relation to GNSS solution only for 5 out of 13 analyzed stations. In the remaining cases, the achieved accuracy is worse than before the GACOS correction.

Figures 8 and Figure 9 represent the time series for the vertical and easting defamation components for various GNSS stations. As can be observed, similar time series behavior is presented for the easting deformation component. This behavior is easily prevalent on the stations which are stable. Therefore, observing the time series, it can be concluded that still some residual error exists in the GACOS corrected LOS deformations and this error can directly reflect easting deformation component (PI04, PI16). The time series of the vertical displacement from DInSAR after GACOS correction corresponds to GNSS quite fairly. However, still some discrepancy exists (TYCH station and

PI04). Probably the application of the additional redundant data from different geometry will increase the results of easing the deformation component. Nevertheless, based on the vertical and horizontal time series, it can be clearly concluded that GACOS increases the accuracy of the SAR measurements.

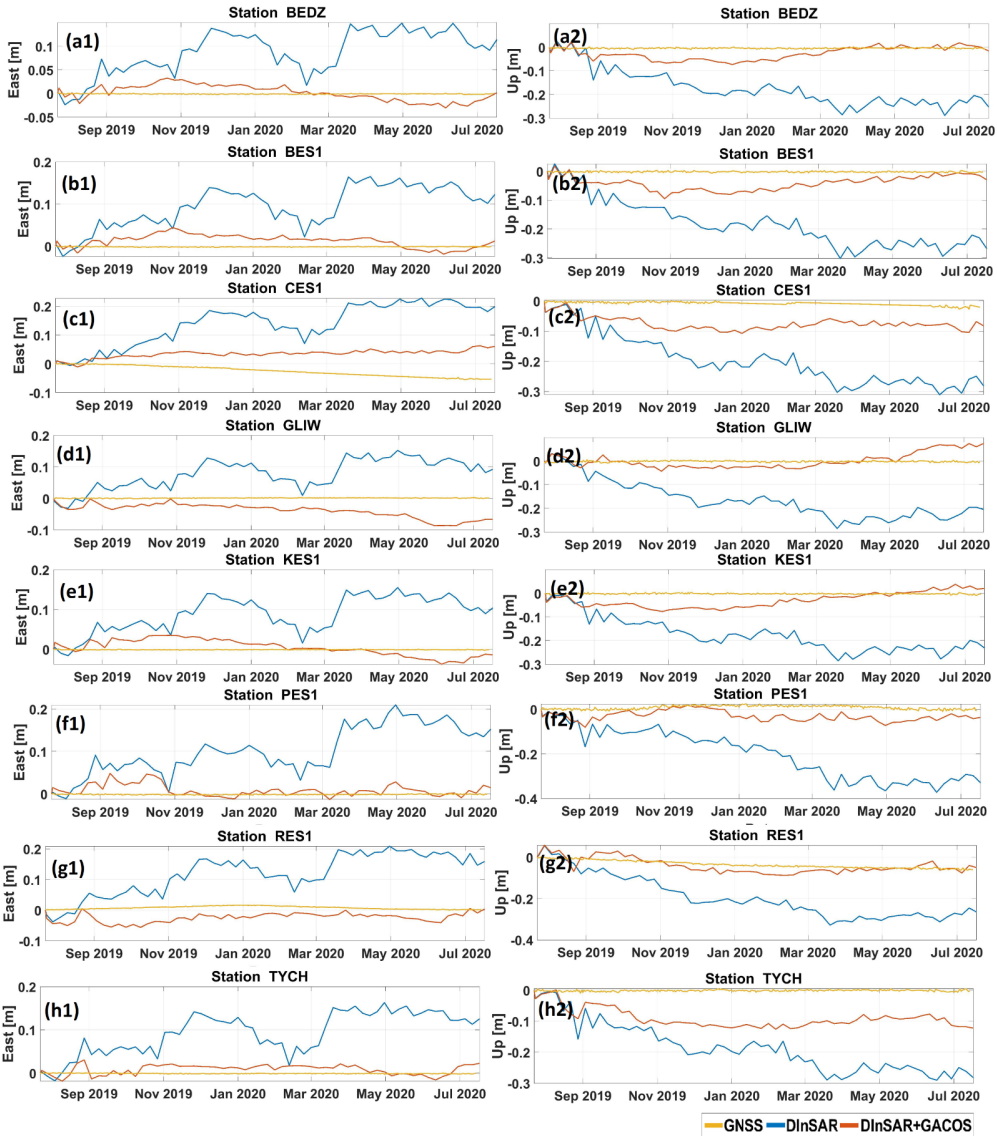

Fig. 8. Time-series for East and Up components from GNSS (yellow line), original DInSAR results (blue) and corrected DInSAR (red) deformation on GNSS station with geodetic grade receivers

Temporal RMSE calculated for the time series for the easting and vertical deformation components also demonstrate clearly the error and deformation variation in time has

been decreased after GACOS. However, based on Figure 10, it is confirmed that a bigger error is represented for the horizontal deformation component rather than for vertical.

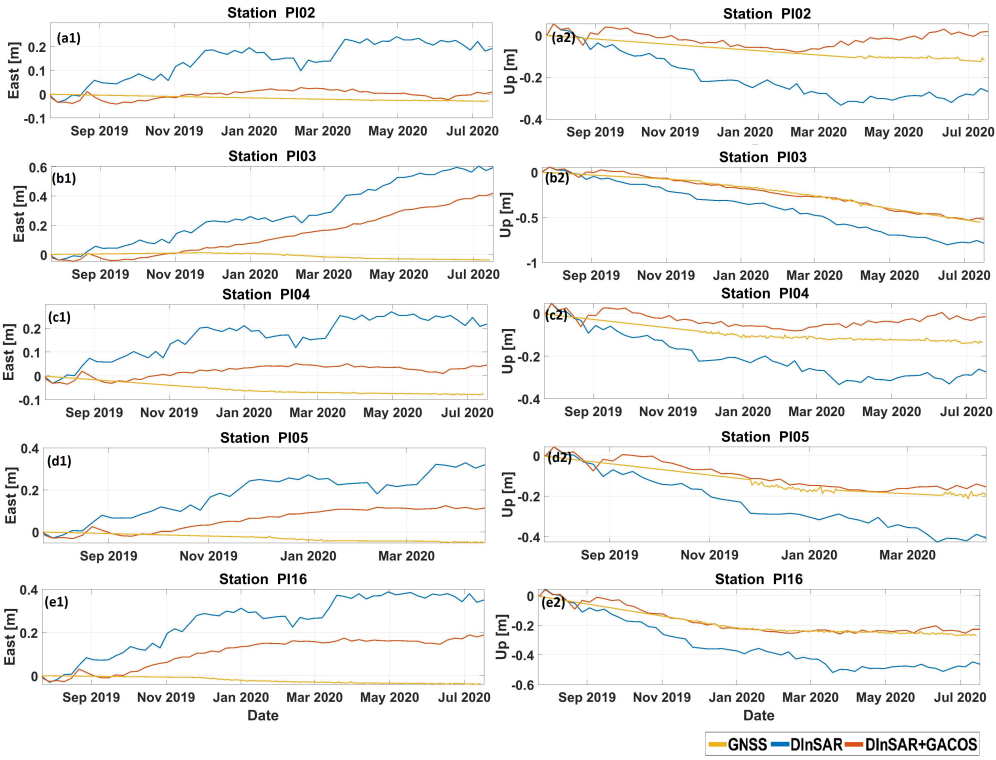

Fig. 9. Time-series for East and Up components from GNSS (yellow line), original DInSAR results (blue) and corrected DInSAR (red) deformation on GNSS station using low-cost

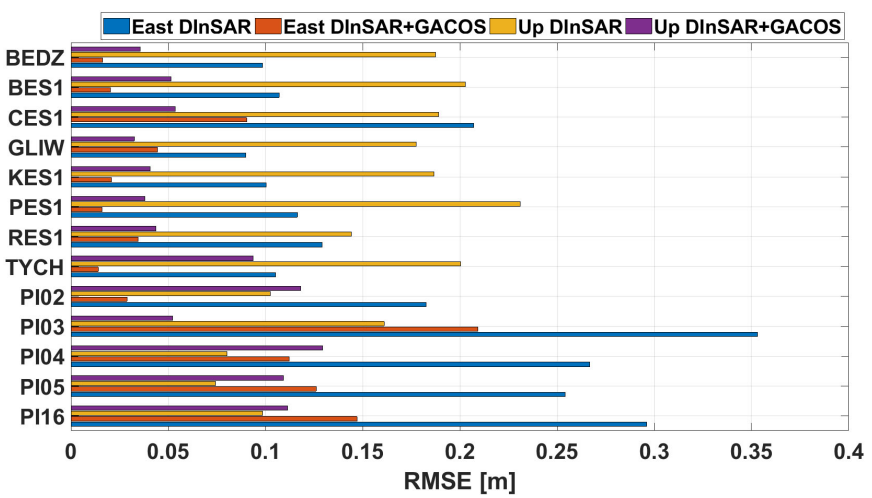

Fig. 10. RMSE for time-series results for East and Up components for each GNSS station

5.3. Single deformation map refinement with the GACOS corrections

A similar analysis was carried out for the cumulative deformation results obtained for approximately 60 interferograms covering the period from the 14th of June 2019 up to 14th of June 2020. The evaluations of the GACOS correction for the accumulated maps were performed for LOS displacement results as well as for results after decomposition in vertical and easting the deformation component. The deformation maps for both geometries before and after the correction are depicted in Figure 11 while the decomposed results are presented in Figure 12.

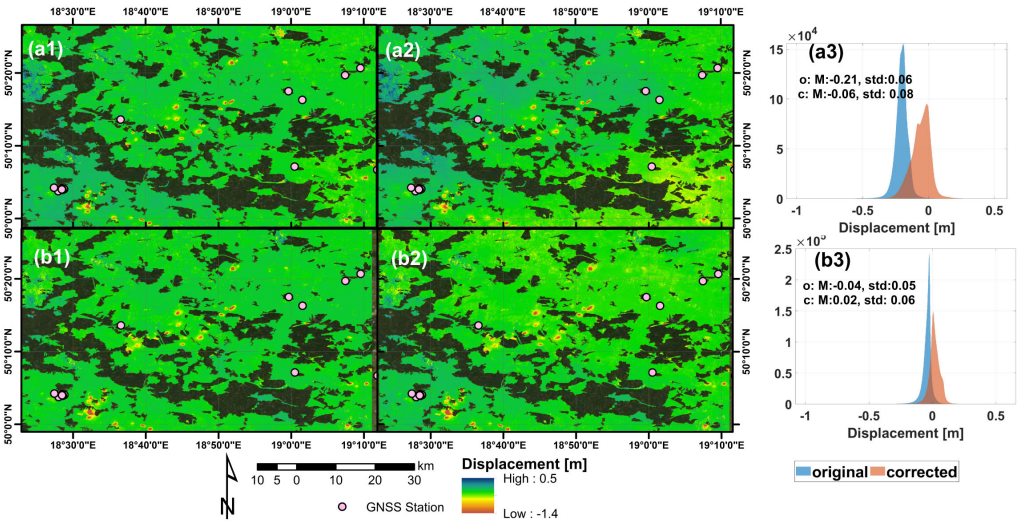

Fig. 11. Deformation in LOS direction, ascending 175 orbits (a) and descending 124 orbits (b). Figures a1–b1 present the original DInSAR results, a2–b2 results after GACOS correction, and a3 and b3 histograms for ascending and descending, geometry

Some small changes in the color variations can be observed on Figure 11a and Figure 11b. However, since the study area is wide and detected deformations cover wide spectrum of the deformations (–1.4 m up to 0.5 m), it is difficult to see GACOS influence in the final deformation maps before and after applying the GACOS correction. Nevertheless, the histograms show that the GACOS atmospheric correction has a positive impact on the final result, especially for the descending orbit (Fig. 11a3). As in the case of single interferograms, a shift of the histograms is visible and the expected value oscillates around 0. This is mostly observable for ascending geometry in Figure 11a3.

Similar situation can be observed in the case of vertical and easting deformation components (Fig. 12). Application of GACOS correction refines the shape of the histogram and the expected values oscillated close to zero. Since the study is large, Figure 13 represents the examples of two mines in Bytom and Ruda Śląska mines. As can be observed from Figure 13, application of GACOS correction minimize some of the horizontal movement. Additionally, the mean difference and RMSE between GNSS re-

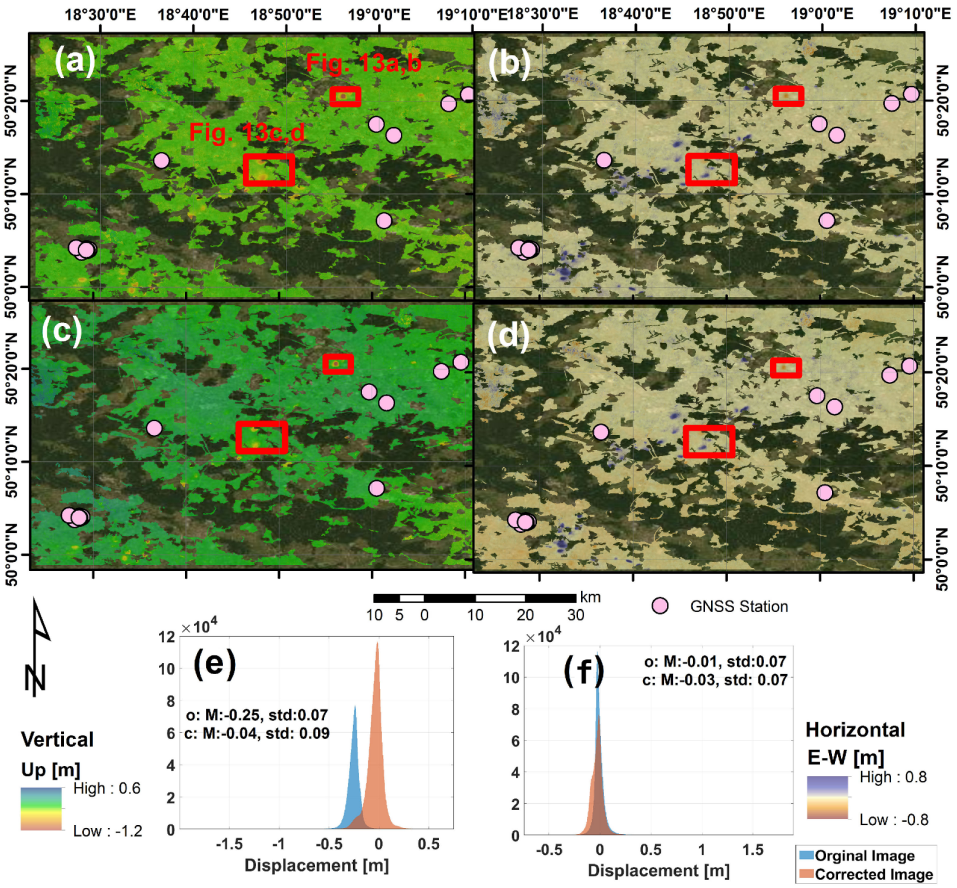

Fig. 12. Vertical (a, c) and horizontal (b, d) deformation. Figures a and b present the original DInSAR the results, c and d present results after GACOS correction

Table 3. Specification of the data used in this study

Parameter	Mean offset [m] (for each station)		RMSE [m]	
	DInSAR	DInSAR+GACOS	DInSAR	DInSAR+GACOS
dsc124 LOS	–0.025	0.056	0.034	0.071
asc175 LOS	–0.178	0.005	0.182	0.052
East	0.233	0.084	0.277	0.157
Up	–0.226	0.019	0.231	0.070

sults and DInSAR are presented in Table 3. As can be observed from the accumulated results for the ascending LOS, easting, and vertical deformation components, GACOS corrections help in atmospheric influence removal. In the case of images in descending orbit, the application of GACOS correction does not improve the cumulative results.

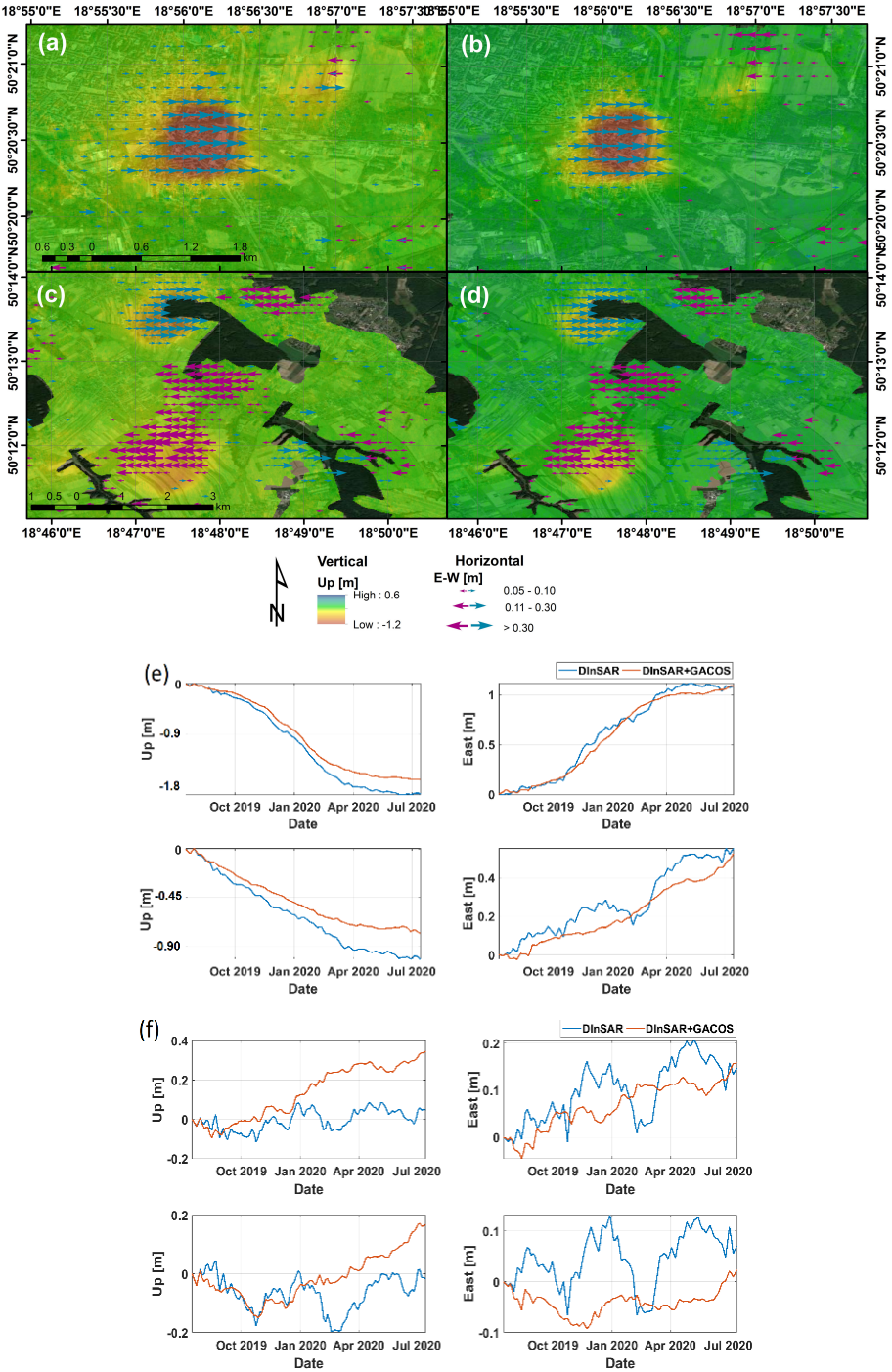

Fig. 13. Vertical (a, c) and horizontal (b,d) deformation for the selected mines in Bytom (a, b) and Ruda Śląska (c,d) before (a,c) and after GACOS correction (b, d) Time series for the selected max vertical displacement point and stable point are presented on e and f respectively

6. Discussion

Many studies evaluated the effect of atmospheric models on interferogram quality, however, these evaluations are mostly carried out using statistical metrics such as the reduction in the overall variance of individual interferograms (e.g. standard deviation, RMSE) (Xiao et al., 2021). In comparison to these studies, we analyzed the improvement in accuracy of GACOS-based DInSAR deformation maps by considering external GNSS data. Based on the authors review, only a few studies evaluated GACOS products with external GNSS data. Wang et al. (2019), showed that the accuracy of deformation monitoring by using SBAS method was improved in the whole investigated study area after GACOS correction, and the mean square error decreased from 0.34 cm/yr to 0.31 cm/yr. Furthermore, Darvishi et al. (2020), assessed methods of reducing atmospheric delay, and GACOS correction with the RMSE of 0.8 cm presented the most precise and accurate results among other Numerical Weather Models.

In the literature, there are also other studies which shows the evaluation of other atmospheric corrections and its comparison with GNSS. Recently, Zebker et al. (2021) proposed model-free approach to minimize the atmospheric artifacts in SBAS processing by using an algorithm that averages the elevation residual phases in every interferogram and compensates for the long-time component of atmospheric variation. They show that a factor of three temporal artifact reduction. For the 11 GPS locations, RMSE decreased from 6.3 cm, 5.2 cm, 4.5 cm to 2.2 cm, 2.0 cm, and 2.4 cm for SBAS solutions with temporal maximum baselines of 12, 30 and 100 days, respectively for the investigated period of January 2018 to November 2018. Another comparison example of the atmospheric correction with GNSS can be correction based on common-point stacking approach presented by Tang et al. (2021). They improved RMSE of 15 mm and 14 mm for ascending and descending orbits, respectively, with 7 mm after atmospheric correction by using SBAS method. On the other hand, Cianflone et al. (2015) using SBAS and removal of atmospheric artefacts with double-pass filtering method achieved RMSE of 1.1 mm/yr and 1.2 mm/yr in comparison to GNSS measurements, respectively for ascending and descending orbits.

Regarding our results, it can be observed that GACOS allows to increase the accuracy of the monitoring, however, the accuracy of SBAS method mentioned before shows significantly better results than DInSAR method. In contrary, sometimes SBAS method cannot be used in the monitoring of sudden and quick phenomena due to the limited number of images since SBAS approach utilized a stack of interferograms. Considering that, our investigation shows that it was possible to achieve RMSE below 1 cm for a single interferogram for only 20% and 26% of the ascending and descending investigated interferograms, respectively. When considering the RMSE below 2 cm, this value increases to 47% and 66% for the descending and ascending interferograms, respectively. In the case of cumulative results of 59 and 61 SAR images, the RMSE changed from 3 cm and 18 cm to 7 cm and 5 m, for descending and ascending geometry, respectively. Thus, GACOS correction has a destructive effect on the descending geometry. Nevertheless, the reason for the negative effect of GACOS correction in descending orbit can be the global character and poor spatial resolution of the used data in GACOS. Wang

et al. (2019) stated that the negative effect can be connected with the turbulent component of the ECMWF weather model, which has a spatiotemporal resolution of 0.125° and 6 h. Slightly better spatial resolution is provided by data derived from the MODIS sensor, where the resolution is about 1 km. However, weather models are limited by a very low temporal resolution. Additionally, GNSS measurements taken with the GACOS correction have various spatial densities and irregularities. According to the GACOS authors, GNSS spatial density varies from 10 km to 200 km (Yu et al., 2018a). Therefore, the density of the GNSS station can directly influence the accuracy of the correction and therefore can be different in various regions on the globe. Unfortunately, it was not possible to find information about which permanent GNSS stations are involved in the GACOS solution in Poland. Based on the fact that it is a free-available service, also the input data are of such character. In Poland, data from GNSS stations, which are part of the EUREF Permanent Network (EPN), are free. In Poland, there are 15 of them, evenly distributed over the country, which means that one GNSS station is available within the radius of about 81 km. Therefore, GNSS stations utilized in this study to evaluate GACOS correction were not included in the GACOS correction estimation. Therefore, in future work, it will be beneficial to take advantage of this additional measurement and better estimate atmospheric artefacts and provide more accurate deformation maps in the USCB. Additionally, considering the phenomena of mining subsidence, which are not sudden, SBAS approach altogether with GACOS correction can be utilized in the future to increase the accuracy of the final solution to mm level. Additionally, it is foreseen that additional data from the third Sentinel-1 orbit will increase the accuracy of the vertical and horizontal deformation components further.

7. Conclusion

The atmospheric effect, mainly connected with the troposphere, is one of the most problematic error sources which directly determine the accuracy of the DInSAR deformation maps. There are numerous methods to minimize its effect. Recently, one of the most popular and widely used corrections is the GACOS service, which provides near real-time and global coverage of atmospheric delay products based on various datasets. In this paper, we analyze the improvement in accuracy of GACOS-based DInSAR deformation maps in reference to external GNSS data. Data evaluation was performed with reference to GNSS measurements from permanent 13 GNSS stations located in the Upper Silesian Coal Basin in Poland. This evaluation was performed for every single interferogram as well as cumulative LOS products and decomposed products in the vertical and easting component.

Generally speaking, GACOS correction had a positive effect on the accuracy of the deformation estimates for every single interferogram as well as the cumulative results generated for GACOS-DInSAR products and for the decomposed results since the errors in every single product were not propagated further. Based on the experiment carried out in this work, it should be expected that the 1 cm error of deformation estimated

is possible to be obtained with a probability of 20–25%, while an error below 2 cm is possible to obtain for with a probability of 47–66%.

Author contributions

Conceptualization: K.P.F.; Methodology development: K.P.F., N.W., T.L., D.T.; Writing – original draft: K.P.F., N.W.; Writing – review and editing: K.P.F., N.W., T.L., D.T.

Data availability statement

Sentinel-1 data are freely available as well as GACOS products are available under request.

Acknowledgements

The presented study was performed thanks to "START2020" scholarship funded by the Foundation for Polish Science and co-financed under the Leading Research Groups support project from the subsidy increased for the period 2020–2025 in the amount of 2% of the subsidy referred to Art. 387 (3) of the Law of 20 July 2018 on Higher Education and Science, obtained in 2019. The research infrastructure which has been used in this project for computation purposes was created within the project EPOS-PL, European Plate Observing System POIR.04.02.00–14-A003/16, funded by the Operational Programme Smart Growth 2014–2020, Priority IV: Increasing the research potential, Action 4.2: Development of modern research infrastructure in the science sector, and co-financed by European Regional Development Fund. The presented paper was performed thanks to the institutions which provided the access to GNSS observations: Military University of Technology (data from low-cost stations PI02, PI03, PI04, PI05 and PI16), Instrumenty Geodezyjne T. Nadowski (data from NadowskiNET network GLIW, JAST and TYCH), ASG-EUPOS (reference data from ASG-EUPOS network).

References

Berardino, P., Fornaro, G., Lanari, R. et. al. (2002). A new algorithm for surface deformation monitoring based on small baseline differential SAR interferograms. *IEEE Trans. Geosci. Remote Sens.*, 40, 2375–2383. DOI: 10.1109/TGRS.2002.803792.

Biagi, L., Grec, F.C., and Negretti, M. (2016). Low-cost GNSS receivers for local monitoring: Experimental simulation, and analysis of displacements. *Sensors*, 16(12), 2140. DOI: 10.3390/s16122140.

Boehm, J., Niell, A., Tregoning, P. et al. (2006). Global Mapping Function (GMF): A new empirical mapping function based on numerical weather model data. *Geophys. Res. Lett.*, 33, 7. DOI: 10.1029/2005GL025546.

Cianflone, G., Tolomei, C., Brunori, C.A. et al. (2015). InSAR time series analysis of natural and anthropogenic coastal plain subsidence: The case of sibari (Southern Italy). *Remote Sens.*, 7, 16004–16023. DOI: 10.3390/rs71215812.

Chen, G. and Herring, T.A. (1997). Effects of atmospheric azimuthal asymmetry on the analysis of space geodetic data. *J. Geophys. Res. Solid Earth*, 102, 20489–20502. DOI: 10.1029/97jb01739.

Dach, R., Lutz, S., Walser, P. et al. (2015). *Bernese GNSS software version 5.2*.

Dach, R., Schaer, S., Arnold, D. et. al. (2018). *CODE final product series for the IGS*. Astronomical Institute, University of Bern.

Darvishi, M., Cuozzo, G., Bruzzone, L. et al. (2020). Performance Evaluation of Phase and Weather-Based Models in Atmospheric Correction with Sentinel-1Data: Corvara Landslide in the Alps. *IEEE J. Sel. Top. Appl. Earth Observ. Remote Sens.*, 13, 1332–1346. DOI: 10.1109/JSTARS.2020.2969726.

Ferretti, A., Prati, C. and Rocca, F. (2001). Permanent scatterers in SAR interferometry. *IEEE Trans. Geosci. Remote Sens.*, 39, 8–20. DOI: 10.1109/36.898661.

Graniczny, M., Kowalski, Z., Przyłucka, M., et al. (2014). Application of SAR data for the monitoring of ground deformations caused by mining activities in the area of the upper Silesian Coal Basin: the results of DORIS project (EC-FP7). *Przegląd Górniczy*, 70(12), 11–19.

Hanssen, R.F. (2001). *Radar interferometry: data interpretation and error analysis*. Springer Science & Business Media.

Li, Z., Fielding, E.J., Cross, P. et al. (2009). Advanced InSAR atmospheric correction: MERIS/MODIS combination and stacked water vapour models. *Int. J. Remote Sens.*, 30(13). DOI: 10.1080/01431160802562172.

Liu, Z., Zhou, C., Fu, H. et. al. (2020). A framework for correcting ionospheric artifacts and atmospheric effects to generate high accuracy InSAR DEM. *Remote Sens*., 12, 318. DOI: 10.3390/rs12020318.

Meyer, F.J., Chotoo, K., Chotoo, S.D. et. al. (2016). The Influence of Equatorial Scintillation on L-Band SAR Image Quality and Phase. *IEEE Trans Geosci Remote Sens.*, 54, 869–880. DOI: 10.1109/TGRS.2015.2468573.

Murray, K.D., Bekaert, D.P.S. and Lohman, R.B. (2019). Tropospheric corrections for InSAR: Statistical assessments and applications to the Central United States and Mexico. *Remote Sens. Environ.*, 232, 111326. DOI: 10.1016/j.rse.2019.111326.

Mutke, G., Kotyrba, A., Lurka, A. et. al. (2019). Upper Silesian Geophysical Observation System. A unit of the EPOS project. *J. Sustain. Min.*, 18, 198–207. DOI: 10.1016/j.jsm.2019.07.005.

Ng, A.H.-M., Ge, L., Zhang, K. et. al. (2011). Deformation mapping in three dimensions for underground mining using InSAR – Southern highland coalfield in New South Wales, Australia. *Int. J. Remote Sens.*, 32, 7227–7256. DOI: 10.1080/01431161.2010.519741.

Notti, D., Cina, A., Manzino, A. et al. (2020). Low-cost GNSS solution for continuous monitoring of slope instabilities applied to Madonna Del Sasso Sanctuary (NW Italy). *Sensors*, 20(1), 289. DOI: 10.3390/s20010289.

Pawluszek-Filipiak, K. and Borkowski, A. (2020). Integration of DInSAR and SBAS techniques to determine mining-related deformations using Sentinel-1 data: The case study of rydultowy mine in Poland. *Remote Sens.*, 12, 242. DOI: 10.3390/rs12020242.

Pawluszek-Filipiak, K. and Borkowski, A. (2021). Monitoring mining-induced subsidence by integrating differential radar interferometry and persistent scatterer techniques. *Eur. J. Remote Sens.*, 54, 18–30. DOI: 10.1080/22797254.2020.1759455.

Perski, Z. (1998). Applicability of Ers-1 and Ers-2 Insar for Land Subsidence Monitoring in the Silesian Coal Mining Region, Poland. *Int. Arch. Photogr. Remote Sens.*, 32, 555–558.

Przylucka, M., Herrera, G., Graniczny, M. et al. (2015). Combination of conventional and advanced DInSAR to monitor very fast mining subsidence with TerraSAR-X data: Bytom City (Poland). *Remote Sens.*, 7, 5300–5328. DOI: 10.3390/rs70505300.

Ramdani, F., Amanda, F.F. and Tsuchiya, N. (2019). *Displacement Linear Surface Rupture of the 2018 Palu Earthquake Detected by Sentinel-1 Sar Interferometry and Very High-Resolution Imageries of Planetscope Data*. In: International Geoscience and Remote Sensing Symposium (IGARSS). Institute of Electrical and Electronics Engineers Inc., pp. 9292–9294.

Razi, P., Tetuko Sri Sumantyo, J., Perissin, D. et al. (2019). Ground deformation measurement of Sinabung vulcano eruption using DInSAR technique. *J. Phys. Conf. Ser.*, 12008. DOI: 10.1088/1742-6596/1185/1/012008.

Tang, W., Zhan, W., Jin, B. et al. (2021). Spatial Variability of Relative Sea-Level Rise in Tianjin, China: Insight from InSAR, GPS, and Tide-Gauge Observations. *IEEE J. Sel. Top. Appl. Earth Obs. Remote Sens.*, 14, 2621–2633. DOI: 10.1109/JSTARS.2021.3054395.

Wang, Q., Yu, W., Xu, B. et al. (2019). Assessing the use of gacos products for sbas-insar deformation monitoring: A case in southern california. *Sensors*, 19, 3894. DOI: 10.3390/s19183894.

Wielgocka, N., Hadas, T., Kaczmarek, A. et al. (2021). Feasibility of Using Low-Cost Dual-Frequency GNSS Receivers for Land Surveying. *Sensors*, 21(6), 1956. DOI: 10.3390/s21061956.

Winsvold, S.H., Kääb, A., Nuth, C. et al. (2018). Using SAR satellite data time series for regional glacier mapping. *Cryosphere*, 12, 867–890. DOI: 10.5194/tc-12-867-2018.

Xiao, R., Yu, C., Li, Z. et al. (2021). Statistical assessment metrics for InSAR atmospheric correction: Applications to generic atmospheric correction online service for InSAR (GACOS) in Eastern China. *Int. J. Appl. Earth Obs. Geoinf.*, 96, 102289. DOI: 10.1016/j.jag.2020.102289.

Yu, C., Penna, N.T. and Li, Z. (2017). Generation of real-time mode high-resolution water vapor fields from GPS observations. *J. Geophys. Res.*, 122, 2008–2025. DOI: 10.1002/2016JD025753.

Yu, C., Li, Z., Penna, N. et al. (2018a). *Generic Atmospheric Correction Online Service for InSAR (GACOS).*

Yu, C., Li, Z., Penna, N.T. (2018b). Interferometric synthetic aperture radar atmospheric correction using a GPS-based iterative tropospheric decomposition model. *Remote Sens. Environ.*, 204, 109–121. DOI: 10.1016/j.rse.2017.10.038.

Yu, C., Li, Z., Penna, N.T. et al. (2018c). Generic Atmospheric Correction Model for Interferometric Synthetic Aperture Radar Observations. *J. Geophys. Res. Solid Earth*, 123, 9202–9222. DOI: 10.1029/2017JB015305.

Yu, C., Li, Z., Penna, N.T. (2020). Triggered afterslip on the southern Hikurangi subduction interface following the 2016 Kaikōura earthquake from InSAR time series with atmospheric corrections. *Remote Sens. Environ.*, 251, 112097. DOI: 10.1016/j.rse.2020.112097.

Zebker, H.A., Rosen, P.A. and Hensley, S. (1997). Atmospheric effects in interferometric synthetic aperture radar surface deformation and topographic maps. *J. Geophys. Res. Solid Earth*, 102, 7547–7563. DOI: 10.1029/96jb03804.

Zebker, H. (2021). Accuracy of a model-free algorithm for temporal insar tropospheric correction. *Remote Sens.*, 13, 1–9. DOI: 10.3390/rs13030409.

Zhou, X., Chang, N.B., Li, S. (2009). Applications of SAR interferometry in earth and environmental science research. *Sensors*, 9, 1876–1912. DOI: 10.3390/s90301876.